Journal of
Marine Science and Engineering

MDPI

Article

Hydrodynamic Shape Optimization of a Naval Destroyer by Machine Learning Methods

Andrea Serani * and Matteo Diez

CNR-INM, National Research Council-Institute of Marine Engineering, 00128 Rome, Italy
* Correspondence: andrea.serani@cnr.it

Abstract: This paper explores the integration of advanced machine learning (ML) techniques within simulation-based design optimization (SBDO) processes for naval applications, focusing on the hydrodynamic shape optimization of the DTMB 5415 destroyer model. The use of unsupervised learning for design-space dimensionality reduction, combined with supervised learning through active learning-based multi-fidelity surrogate modeling, allows for significant improvements in computational efficiency while addressing complex, high-dimensional design spaces. By applying these ML techniques to both single- and multi-objective optimizations, aimed at minimizing resistance and enhancing seakeeping performance, the proposed framework demonstrates its practical value in hydrodynamic design. This approach provides a scalable and efficient solution, reducing the reliance on high-fidelity simulations while accelerating the optimization process, without substantial modifications to existing toolchains. A design-space dimensionality reduction of approximately 70% is achieved, reducing the design variables from 22 to 7 while retaining 95% of the original geometric variance. Additionally, computational cost reductions of 65% to 98% are observed, compared to using the full design space and high-fidelity simulations only.

Keywords: simulation-based design; shape optimization; ship hydrodynamics; multi-fidelity; surrogate modeling; dimensionality reduction; active learning; representation learning

Citation: Serani, A.; Diez, M. Hydrodynamic Shape Optimization of a Naval Destroyer by Machine Learning Methods. *J. Mar. Sci. Eng.* **2024**, *12*, 1979. https://doi.org/10.3390/jmse12111979

Academic Editor: Apostolos Papanikolaou

Received: 18 September 2024
Revised: 22 October 2024
Accepted: 29 October 2024
Published: 2 November 2024

1. Introduction

Hydrodynamic shape optimization plays a pivotal role in the design of ships and in particular naval destroyers, where performance characteristics such as speed, maneuverability, seakeeping, fuel efficiency, and operational effectiveness are critical. Ship hydrodynamic efficiency significantly influences its operational capabilities, environmental footprint, and overall cost-effectiveness. Thus, achieving optimal hull shapes can result in significant fuel savings and reduce greenhouse gas emissions, a pressing concern in the context of modern naval engineering [1].

A recent review [2] has highlighted a significant shift in the naval engineering sector, which, for decades, relied predominantly on experimental campaigns and semi-empirical approaches. Over the last twenty years, the industry has increasingly adopted simulation-based design optimization (SBDO), aligning its methodologies with those used in the aeronautical and automotive sectors. This transition marks a change of course from the traditional design, build, and test approach toward more modern, simulation-driven paradigms, where optimization plays a central role in improving performance while reducing costs and time-to-market.

Despite this "methodological revolution", the adoption of advanced techniques remains slower than expected. As shown in [2], the use of cutting-edge tools such as machine learning (ML) in marine engineering is still limited compared to sectors like aerospace engineering. The aeronautical industry, for instance, has embraced ML technologies [3] to enhance the efficiency of optimization processes, particularly in handling complex, high-dimensional design problems. In contrast, the naval sector has been more conservative in

integrating these innovations into standard practices. Nonetheless, some recent examples are also available in the marine sector, such as the use of neural networks for the prediction of the resistance of containerships [4] and trimarans [5], ship motions [6], the power and emission of different vessels [7], as well as mooring system dynamics [8].

The objective of this paper is to illustrate how ML techniques can be seamlessly integrated into SBDO processes for naval applications, enhancing the workflow without requiring significant modifications to existing toolchains. Specifically, attention is focused on two key ML approaches. First, unsupervised learning techniques, such as parametric model embedding (PME) [9], are used to reduce the dimensionality of the design space upfront. This addresses the well-known "curse of dimensionality" [10], a challenge that severely impacts the performance and convergence of both surrogate models and optimization algorithms as the number of design variables increases. By embedding the original high-dimensional design space into a lower-dimensional representation, the most relevant design features are retained, enabling a more efficient exploration of the design space without disrupting the existing SBDO workflow. Second, supervised learning techniques in the form of active learning-based multi-fidelity surrogate models [11] are integrated into the optimization process. These models, designed to predict hydrodynamic performance based on both low- and high-fidelity simulations, refine themselves selectively during the optimization process. This approach minimizes the need for computationally expensive high-fidelity simulations by leveraging active learning [12] to focus on the most critical areas of the design space. Notably, these ML-driven surrogate models, herein based on stochastic radial basis functions (RBF) [13] can be easily incorporated into the SBDO process, improving the workflow by accelerating certain stages of optimization without necessitating a complete overhaul of existing methods.

The test case considered focuses on the hydrodynamic shape optimization of a naval destroyer, specifically the DTMB 5415 model. This benchmark model has been widely used in international literature for experimental [14], numerical [15], and optimization [16] studies. The application of both single- and multi-objective optimization techniques to this test case aims to demonstrate how ML techniques can be effectively integrated into existing SBDO toolchains, paving the way for broader adoption of these advanced methods in the naval sector.

The remainder of this paper is organized as follows. Section 2 presents the hydrodynamic test case, focusing on the DTMB 5415 model, its specifications, and its role as a benchmark for naval destroyer optimization. Section 3 outlines the formulation of the hydrodynamic shape optimization problems, detailing both single-objective and multi-objective approaches for minimizing resistance and improving seakeeping performance, as well as, design parameterization and numerical solvers. Section 4 describes the ML methods used in the optimization process, including PME for design-space dimensionality reduction and active learning-based surrogate models for multi-fidelity optimization, and illustrates how they can be easily integrated into existing SBDO workflows. Section 5 presents the results obtained using these techniques and, finally, Section 6 offers concluding remarks, summarizing the key findings and potential future developments for the use of ML in hydrodynamic shape optimization.

2. Ship Hydrodynamic Test Case

The DTMB 5415 model, derived from a series developed by the David Taylor Model Basin (now known as the Naval Surface Warfare Center, Carderock Division), has long been a cornerstone in naval architecture research. This model represents a destroyer-type vessel and has been extensively utilized within both academic and practical settings to explore and enhance ship hydrodynamics [17]. With its origins tracing back to the mid-20th century, the DTMB 5415 model has provided a reliable platform for numerous studies, owing to its well-documented hydrodynamic characteristics and performance in calm water and real seas conditions [18].

This model is particularly noted for its operational specifications, which are meticulously designed to replicate the hydrodynamic behavior of full-scale DDG-51 vessels under various conditions (see Figure 1, left). The model's specifications, summarized in Table 1, include a standard length of approximately 5.72 m, with a beam of 0.76 m, and a draft of 0.248 m, at nominal conditions. This scale model ($\lambda = 24.8$) is characterized by a specific Froude number (Fr) of 0.28, making it ideal for studies focusing on calm-water resistance and other hydrodynamic performances, such as seakeeping [19] and maneuvering [20].

Figure 1. Starboard bow view of the Arleigh Burke-class guided missile destroyer (DDG-51, **left**) alongside its digital counterpart, the DTMB 5415 model (**right**).

Table 1. Key characteristics of the DTMB 5415 original hull and simulation parameters.

Quantity	Symbol	Unit	Value
Displacement	∇	m^3	0.549
Length between perpendiculars	L_{pp}	m	5.720
Beam	B	m	0.760
Draft	T	m	0.248
Longitudinal center of gravity	LCG	m	2.884
Vertical center of gravity	VCG	m	0.056
Bridge longitudinal location	b_x	m	1.772 †
Bridge vertical location	b_z	m	0.997 ‡
Flight deck longitudinal location	d_x	m	5.317 †
Flight deck vertical location	d_z	m	0.524 ‡
Roll radius of gyration	K_{xx}	–	$0.40B$
Pitch radius of gyration	K_{yy}	–	$0.25L_{pp}$
Yaw radius of gyration	K_{zz}	–	$0.25L_{pp}$
Water density	ρ	kg/m^3	998.5
Kinematic viscosity	ν	m^2/s	1.09×10^{-6}
Gravity acceleration	g	m/s^2	9.803
Froude number	Fr	–	0.280

† backward bow, ‡ above the keel.

In the scholarly domain, the DTMB 5415 has been employed as a fundamental test case for a myriad of research initiatives [21]. It has significantly contributed to experimental hydrodynamics and computational fluid dynamics (CFD) [22,23], serving as a reliable benchmark for testing and validating new theories and computational models [24,25]. The literature cites its use in various contexts, including the verification of numerical simulation techniques [26] and the development of new experimental methodologies [27,28]. More recently, the DTMB 5415 model has been at the forefront of advancing multi-fidelity methods for ship design optimization [29,30] and used as so-called L2 and L3 sea benchmark problems to develop and assess multi-fidelity optimization methods for military vehicle design within the AVT-331 Research Task Group on "Goal-driven, multi-fidelity approaches for military vehicle system-level design" [31].

3. Hydrodynamic Shape Optimization Problems

The general framework for design optimization can be formulated as follows:

$$\begin{array}{rll} \text{minimize} & f_k(\mathbf{u}) & \text{for} \quad k = 1, \ldots, K \\ \text{subject to} & h_i(\mathbf{u}) = 0 & \text{for} \quad i = 1, \ldots, I \\ \text{and} & g_j(\mathbf{u}) \leq 0 & \text{for} \quad j = 1, \ldots, J \\ & \mathbf{u}_l \leq \mathbf{u} \leq \mathbf{u}_u & \end{array} \tag{1}$$

where $\mathbf{u} \in \mathbb{R}^M$ represents the vector of design variables, with M denoting the number of variables that govern the shape parameterization of the hull. The lower and upper bounds on the design variables are denoted by $\mathbf{u}_l$ and $\mathbf{u}_u$, respectively. The objective functions, f_k, address either a single-objective ($k = 1$) or multi-objective ($k > 1$) problem, depending on the complexity of the desired optimization task. The equality constraints are represented by h_i, while the inequality constraints are described by g_j. These constraints ensure that the design remains feasible and adheres to the physical and engineering limitations imposed by the problem.

In this study, two distinct optimization problems are addressed, considering two operational scenarios: calm water and regular wave conditions. The design objectives focus on two primary performance criteria: (i) resistance minimization in calm water and in waves, and (ii) seakeeping performance, which evaluates the ship's motion responses under wave action. The hydrodynamic and seakeeping of the vessel are coupled through physical models, accounting for rigid body motion only. The rigid body equations of motion are used to compute the dynamic response of the vessel, while the hydrodynamic models (such as potential flow or Reynolds-averaged Navier–Stokes—RANS) provide the necessary force and moment inputs.

Herein, the problem formulation includes a set of equality h_i and inequality g_j constraints designed to ensure that the optimized hull configurations remain practical, as specified in the following

$$\begin{cases} h_1 = L_{\text{pp}}(\mathbf{u})/L_{\text{pp}_0} - 1 \\ g_1 = 1 - \nabla(\mathbf{u})/\nabla_0 \\ g_2 = |\Delta B(\mathbf{u})|/B_0 - 0.05 \\ g_3 = |\Delta T(\mathbf{u})|/T_0 - 0.05 \\ g_4 = 1 - V(\mathbf{u})/V_0 \end{cases} \tag{2}$$

The length between perpendiculars is fixed as an equality constraint to ensure that the optimized designs maintain the overall ship length. The inequality constraints pertain to the vessel's displacement, beam, draft, and sonar dome volume, ensuring that the displacement is at least equal to that of the reference hull while allowing a permissible variation in beam and draft of $\pm 5\%$, as well as a minimum volume V_0 within the bow dome to contain the sonar. This variation enables flexibility in the design space without sacrificing critical performance or stability requirements.

3.1. Single- and Multi-Objective Formulations

Problem 1 is formulated as a single-objective optimization problem ($k = 1$) aimed at minimizing the total resistance (R_T) of the ship in calm water at a Froude number of 0.28, which corresponds to a full-scale speed of 20 knots. The optimization objective is expressed as

$$\text{minimize} \quad f_1(\mathbf{u}) = R_\text{T}(\mathbf{u}) \tag{3}$$

The objective function, $R_\text{T}(\mathbf{u})$, quantifies the resistance exerted on the ship. This problem is particularly relevant for reducing fuel consumption and improving the overall energy efficiency of the vessel.

Problem 2 is a multi-objective optimization problem ($k = 2$) designed to simultaneously reduce the resistance and enhance the seakeeping performance of the ship when

operating in regular head waves. The Froude number remains fixed at $Fr = 0.28$. The two objectives are defined as follows:

$$\begin{aligned} &\text{minimize} \quad f_1(\mathbf{u}) = \bar{R}_\mathrm{T}(\mathbf{u}) = \tfrac{1}{T_e}\int_0^{T_e} R_\mathrm{T}(\mathbf{u}, t)\,\mathrm{d}t \\ &\text{minimize} \quad f_2(\mathbf{u}) = \mathrm{SMF}(\mathbf{u}) = \tfrac{1}{3}\tfrac{\mathrm{RMS}(v_d)}{\mathrm{RMS}(v_{d,0})} + \tfrac{1}{3}\tfrac{\mathrm{RMS}(a_b)}{\mathrm{RMS}(a_{b,0})} + \tfrac{1}{3}\tfrac{\mathrm{RMS}(\theta)}{\mathrm{RMS}(\theta_0)} \end{aligned} \tag{4}$$

In this case, $\bar{R}_\mathrm{T}(\mathbf{u})$ represents the time-averaged resistance over the encounter wave period T_e, where the resistance varies with time due to the dynamic nature of the wave environment. The regular waves are characterized by a wavelength-to-ship-length ratio $\lambda/L_\mathrm{pp} = 1.2$ and a wave steepness $H/\lambda = 1/30$. The second objective, $f_2(\mathbf{u})$, is a seakeeping merit factor (SMF), which evaluates the ship's motion responses in waves, focusing on three key metrics: the vertical velocity at the flight deck (v_d), the vertical acceleration at the bridge (a_b), and the pitch angle (θ). Each of these metrics is normalized by their corresponding values for the parent hull, denoted by the subscript '0'. The SMF is calculated as the weighted average of the root mean square (RMS) values of these three responses, each contributing equally to the overall seakeeping performance.

The multi-objective nature of Problem 2 inherently involves trade-offs between reducing resistance and improving seakeeping performance, as design changes that benefit one objective may negatively impact the other. The use of a multi-objective framework allows for the identification of a set of non-dominated, or Pareto-optimal, solutions where neither objective can be improved without compromising the other. This approach provides greater flexibility in selecting a hull design that balances operational efficiency and seakeeping with onboard comfort and safety in rough seas.

3.2. Hull-Form Parameterization

Free-form deformation (FFD) [32] is utilized to generate design variations and modify the corresponding computational grid. The control points, which act as lattice nodes, are strategically placed to enable both local and global modifications of the hull geometry. The selection of the number and positioning of these control points is informed by prior research and practical experience [33], ensuring an effective and flexible design process.

The design space for the hull optimization is represented by a total of $M = 22$ design variables. The demi-hull is embedded in a lattice structure composed of $9 \times 3 \times 3$ nodes. It is important to note that the FFD lattice is tailored to fit the maximum dimensions of the demi-hull, allowing precise control over the shape modifications. Out of the total nodes, 21 are considered active (indicated by the blue spheres in Figure 2), each of which has one degree of freedom (DoF), except for one node that possesses two DoF. The overall shape modification is achieved by interpolating the control points' displacements across the lattice grid.

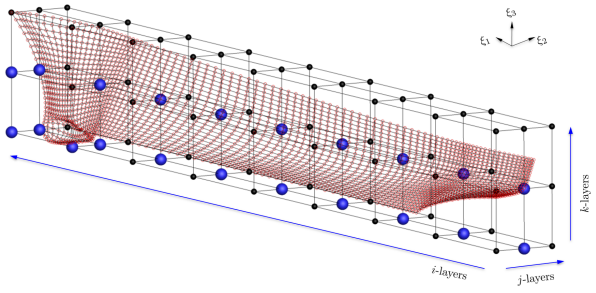

Figure 2. FFD parameterization.

This interpolation process can be executed using various polynomial bases. In this work, a tensor product of trivariate Bernstein polynomials is employed, which allows for smooth and continuous shape modifications. A detailed description of the degrees of freedom and the associated design variables can be found in [9].

This approach allows for a flexible and efficient design process, enabling the exploration of both subtle and substantial modifications to the hull shape. The use of FFD in conjunction with polynomial interpolation provides the necessary smoothness and continuity required for hydrodynamic optimization while maintaining computational efficiency.

3.3. Physical Models and Numerical Solvers

Several governing equations and computational solvers, each utilizing different grid resolutions, are employed to support the multi-fidelity supervised learning approach used in solving the design optimization problems. Each solver operates at a different fidelity level, providing varying degrees of accuracy and computational cost. By integrating these solvers within the multi-fidelity framework, it becomes possible to balance computational efficiency with precision, leveraging both high-fidelity and low-fidelity models.

In the following, a brief overview of the models, codes, and computational setups used in this multi-fidelity approach is provided. Each model and solver has been tailored to address specific aspects of the problem, ranging from potential flow simulations for rapid low-fidelity evaluations to more detailed RANS solvers for high-fidelity simulations. This combination ensures that the most computationally demanding simulations are only used where necessary, while less expensive solvers are employed for broader design space exploration.

3.3.1. CFDShip-Iowa

Resistance and seakeeping performance at high fidelity (HF) are evaluated by the CFDShip-Iowa V4.5 code [34], developed at the University of Iowa over the last three decades. It is a specialized solver for incompressible URANS/DES equations tailored to ship hydrodynamics. The equations are solved in an inertial reference frame attached to the ship, assuming constant speed. The free surface is handled through a single-phase approach, where only the water flow is simulated, with kinematic and dynamic boundary conditions applied at the free surface. The software utilizes structured multiblock grids and features overset grid capabilities.

Turbulence modeling is based on the blended Menter's k-ω/k-ϵ model with shear stress transport. A second-order upwind scheme is employed to discretize the convective terms of the momentum equations. For pressure and velocity coupling, a projection method [35] is applied. Additionally, the SUGGAR code [36] operates separately from the main solver to compute interpolation coefficients for the overset grids, enabling the simulation of 6DoF, with a motion controller active at each timestep.

Here, the computational domain consists of a background grid with 3.5 million points and a boundary layer grid with approximately 1 million points, designed to exploit the symmetry of the problem. The background grid extends from $0.5L_{\mathrm{pp}}$ upstream to $2L_{\mathrm{pp}}$ downstream, and laterally to $2L_{\mathrm{pp}}$, while vertically it extends $1.7L_{\mathrm{pp}}$ below the waterline and $0.3L_{\mathrm{pp}}$ above. The boundary layer grid is carefully refined to ensure $y^{+} < 1$, thereby eliminating the need for wall functions. A detailed view of the computational grid is presented in Figure 3 (left). Notably, the background grid is configured for seakeeping simulations, as the seakeeping merit factors are evaluated after the calm-water solution has converged. To achieve this, the grid discretizes both wavelength and wave height into 100 points, and the computational time is divided into 256 steps to capture one full encounter wave period.

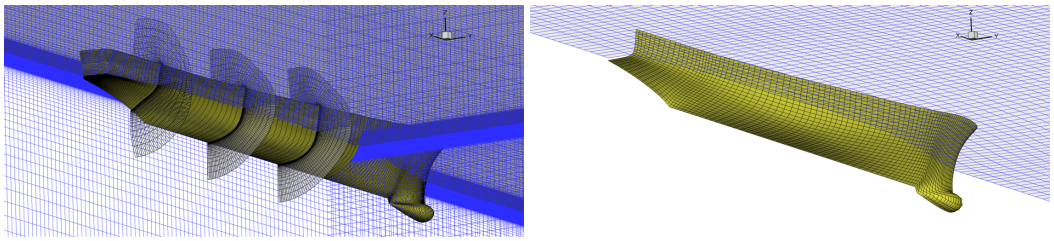

Figure 3. Computational grids used for the high-fidelity solver (**left**, CFDShip-Iowa with URANS) and low-fidelity solver (**right**, WARP using potential flow).

3.3.2. WARP

Resistance value in calm water at low fidelity (LF) is evaluated by the wave resistance program (WARP), a linear potential-flow (PF) solver developed at CNR-INM (previously known as INSEAN). The computation of wave resistance is based on Dawson's linearization technique using the double-model approach [37], while frictional resistance is approximated using a flat-plate model that incorporates the local Reynolds number [38]. The total resistance is calculated by integrating pressure and friction forces over the surface of the hull. The program achieves a steady-state solution for sinkage and trim (2DoF) through iterative coupling between the flow solver and the equations governing the body's motion. Further details on the equations, numerical implementations, and validations of the solver can be found in previous work [39].

Here, the computational domain includes a free-surface grid with 7600 points and a hull surface grid with 9000 points, both leveraging the symmetry of the problem. The free-surface grid extends $1L_{pp}$ upstream, $3L_{pp}$ downstream, and $1.5L_{pp}$ laterally, resulting in a total grid resolution of 75×20 nodes. A detailed view of the computational grid is provided in Figure 3 (right).

3.3.3. SMP

The seakeeping performance at low fidelity is evaluated using the standard ship motion program (SMP), developed by the David Taylor Naval Ship Research and Development Center [40]. SMP employs a potential flow model that uses linearized strip theory to predict ship motions in the frequency domain. The program calculates the 6DoF response of the vessel, considering constant forward speed and arbitrary heading angles. It is capable of simulating both regular waves and irregular sea conditions. The response data provided includes longitudinal, lateral, and vertical motions at specific points on the ship, offering insight into how the vessel behaves under various seakeeping conditions. SMP is widely used for preliminary seakeeping analysis due to its ability to balance computational efficiency with reasonably accurate predictions, making it an effective tool for early-stage design assessments where full-scale simulations would be too computationally expensive.

Simulations using the SMP code are carried out by utilizing the symmetry of the hull. The hull is divided into 31 strips, with each strip further discretized into 10 nodes, uniformly distributed along the curvilinear coordinate of the strip.

4. Machine Learning Methods

This section presents the two ML techniques employed in this work: unsupervised learning through PME for reducing the dimensionality of the design space, and supervised learning via active learning-based multi-fidelity surrogate modeling. Both approaches integrate seamlessly into a traditional SBDO workflow, enhancing the process's ability to handle complex, high-dimensional design spaces while simultaneously reducing the dependence on computationally intensive high-fidelity simulations. As shown in Figure 4, a schematic comparison illustrates the differences between the standard SBDO approach and the ML-enhanced shape optimization workflow.

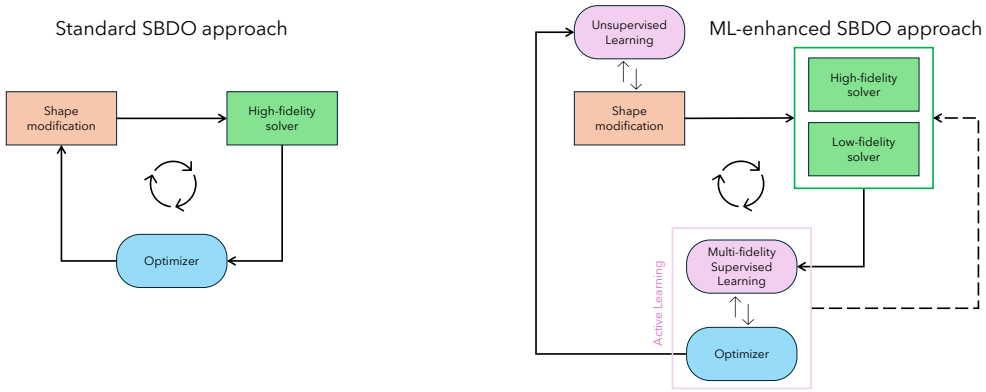

Figure 4. ML-based shape optimization flow chart compared to standard SBDO.

In contrast to the standard SBDO process, where the full design space is used throughout the optimization, unsupervised learning via PME is applied upfront to reduce the dimensionality of the design space. This step preserves a direct mapping to the original parameterization (see later Equation (14)), ensuring that the critical features of the design are maintained. By reducing the complexity of the design space before entering the optimization loop, PME enables the continued use of the original shape modification methods, such as FFD, but with a more efficient and manageable parameterization.

Once the design space is reduced, the optimization process in Equation (1) is solved in the reduced design space using a multi-fidelity surrogate model $\hat{f}(\mathbf{x})$ (see later Equation (18)). This model integrates information from both low- and high-fidelity simulations, starting with a few points from each fidelity level. Initially, only one high-fidelity point is placed at the center of the design space, and the active learning procedure determines both where to sample new points and which fidelity level to use. The decision is guided by balancing the uncertainty of the predictions from each model against the computational cost of the simulations. This approach significantly reduces the number of costly high-fidelity evaluations needed by efficiently focusing computational resources on the most critical areas of the design space [41]. The optimization is performed directly on the surrogate model, which approximates the objective functions and constraints. Active learning thus ensures that the optimization process remains efficient and accurate, minimizing computational expense without sacrificing precision.

By fusing the strengths of PME for dimensionality reduction and active learning for efficient sampling in multi-fidelity models, this approach offers a robust framework for tackling complex hydrodynamic shape optimization problems. The result is a streamlined and computationally efficient process compared to traditional methods, without sacrificing the accuracy or robustness required in naval engineering applications.

4.1. Unsupervised Learning via Parametric Model Embedding for Design-Space Dimensionality Reduction

PME [9] is a design-space dimensionality reduction method that extends the standard principal component analysis (PCA) approach [42] by incorporating both shape deformations and design variables into a generalized feature space [43]. Specifically, PME applies PCA to an augmented matrix that includes the discretized shape deformation vector $\mathbf{d}$ and the original design variables $\mathbf{u}$. This extension allows PME to directly map the reduced design space back to the original design variables without the need for reparameterization, which is typically required in standard PCA approaches. As a result, PME offers a more robust and practical method for maintaining the integrity of the original design features while facilitating effective shape optimization.

Consider a manifold $\mathcal{G}$, which identifies the original/parent shape. This manifold defines the geometric space in which the shape is parameterized by curvilinear coordinates

$\boldsymbol{\xi} \in \mathcal{G}$. The coordinates of the original shape are represented by $\mathbf{g}(\boldsymbol{\xi}) \in \mathbb{R}^n$ with $n = 1, 2$, or 3. Assume that, for the purpose of shape optimization, $\mathbf{g}$ can be transformed to a deformed shape/geometry $\mathbf{g}'(\boldsymbol{\xi}, \mathbf{u})$ by

$$\mathbf{g}'(\boldsymbol{\xi}, \mathbf{u}) = \mathbf{g}(\boldsymbol{\xi}) + \delta(\boldsymbol{\xi}, \mathbf{u}) \qquad \forall \boldsymbol{\xi} \in \mathcal{G} \tag{5}$$

where $\delta(\boldsymbol{\xi}, \mathbf{u}) \in \mathbb{R}^n$ is the resulting shape modification vector, defined by arbitrary shape parameterization or modification method (e.g., CAD parameterization, Bezier surfaces, FFD, NURBS, etc.), and $\mathbf{u} \in \mathcal{U} \subset \mathbb{R}^M$ is the design variable vector.

Discretizing $\mathcal{G}$ by L elements of measure $\Delta\mathcal{G}_j$ (with $j = 1, \ldots, L$), having $\mathbf{d}(\boldsymbol{\xi}, \mathbf{u})$ as the discretization of $\delta(\boldsymbol{\xi}, \mathbf{u})$, sampling $\mathcal{U}$ by a statistically convergent number of Monte Carlo realizations S, so that $\{\mathbf{u}_k\}_{k=1}^{S} \sim p(\mathbf{u})$, and organizing $\hat{\mathbf{d}} = \mathbf{d} - \langle \mathbf{d} \rangle$ (with $\langle \cdot \rangle$ the mean value) in a data matrix $\mathbf{D}$ of dimensionality $[nL \times S]$

$$\mathbf{D} = \begin{bmatrix} \hat{d}_{1,\xi_1}(\mathbf{u}_1) & & \hat{d}_{1,\xi_1}(\mathbf{u}_S) \\ \vdots & & \vdots \\ \hat{d}_{L,\xi_1}(\mathbf{u}_1) & & \hat{d}_{L,\xi_1}(\mathbf{u}_S) \\ \vdots & \cdots & \vdots \\ \hat{d}_{1,\xi_n}(\mathbf{u}_1) & & \hat{d}_{1,\xi_n}(\mathbf{u}_S) \\ \vdots & & \vdots \\ \hat{d}_{L,\xi_n}(\mathbf{u}_1) & & \hat{d}_{L,\xi_n}(\mathbf{u}_S) \end{bmatrix} \tag{6}$$

where $\hat{d}_{j,\xi_k}$ is the k-th component of the shape modification vector associated to the j-th element, defining $\hat{\mathbf{u}} = \mathbf{u} - \langle \mathbf{u} \rangle$, the embedding is achieved defining the matrix $\mathbf{P}$ of dimensionality $[(nL + M) \times S]$ as follows

$$\mathbf{P} = \begin{bmatrix} \mathbf{D} \\ \mathbf{U} \end{bmatrix} \qquad \text{with} \qquad \mathbf{U} = \begin{bmatrix} \hat{u}_{1,1} & & \hat{u}_{1,S} \\ \vdots & \cdots & \vdots \\ \hat{u}_{M,1} & & \hat{u}_{M,S} \end{bmatrix} \tag{7}$$

where the matrix $\mathbf{U}$ is added to the data matrix $\mathbf{D}$ to which is associated a null weight $\mathbf{W_u}$ such that

$$\mathbf{W_u} = \mathbf{0} \qquad \text{and} \qquad \widetilde{\mathbf{W}} = \begin{bmatrix} \mathbf{W} & \mathbf{0} \\ \mathbf{0} & \mathbf{W_u} \end{bmatrix} \tag{8}$$

and so leading to a generalized PCA problem in the form

$$\widetilde{\mathbf{A}}\widetilde{\mathbf{G}}\widetilde{\mathbf{W}}\widetilde{\mathbf{Z}} = \widetilde{\mathbf{Z}}\widetilde{\mathbf{\Lambda}} \qquad \text{with} \qquad \widetilde{\mathbf{A}} = \frac{1}{S}\mathbf{P}\mathbf{P}^{\mathsf{T}} \tag{9}$$

where

$$\widetilde{\mathbf{G}} = \begin{bmatrix} \mathbf{G} & \mathbf{0} \\ \mathbf{0} & \mathbf{I} \end{bmatrix} \qquad \text{and} \qquad \widetilde{\mathbf{Z}} = [\tilde{\mathbf{z}}_1 \ \ldots \ \tilde{\mathbf{z}}_S] \qquad \text{with} \qquad \tilde{\mathbf{z}}_k = \begin{bmatrix} \mathbf{z}_k \\ \mathbf{v}_k \end{bmatrix} \tag{10}$$

Here, $\mathbf{z}_k$ and $\mathbf{v}_k$ represent the eigenvector components associated to the shape modification $\mathbf{d}$ and design variable $\mathbf{u}$ vectors, respectively. The matrix $\mathbf{G} = \text{diag}(\mathbf{G}_1, \ldots, \mathbf{G}_n)$ is block diagonal and has dimensionality $[nL \times nL]$, with each $[L \times L]$ k-th block being a diagonal matrix itself

$$\mathbf{G}_k = \text{diag}(\Delta\mathcal{G}_1, \ldots, \Delta\mathcal{G}_L) \tag{11}$$

containing the measure $\Delta\mathcal{G}_j$ of the j-th element. Similarly, $\mathbf{W} = \text{diag}(\mathbf{W}_1, \ldots, \mathbf{W}_n)$ is a block diagonal matrix of dimensionality $[nL \times nL]$, where each $[L \times L]$ k-th block $\mathbf{W}_k$ ($k = 1, \ldots, n$) is itself a diagonal matrix defined as

$$\mathbf{W}_k = \text{diag}(\rho_1, \ldots, \rho_L) \tag{12}$$

Here, ρ_j (for $j = 1, \ldots, L$) represents the arbitrary weight given to each element.

The solutions λ_k and $\tilde{\mathbf{z}}_k$ of Equation (9) are finally used to construct the reduced dimensionality representation of the original parameterization; defining the desired confidence level l, with $0 < l \leq 1$, the number of reduced design variables N is chosen such that

$$\sum_{k=1}^{N} \lambda_k \geq l \sum_{k=1}^{nL} \lambda_k = l\sigma^2 \quad \text{with} \quad \lambda_k \geq \lambda_{k+1} \tag{13}$$

and the PME of the original design variables is finally achieved by using the eigenvector components $\mathbf{v}_k$ that embed (or contain) the reduced-order representation of the original design parameterization $\mathbf{u}$ as follows

$$\mathbf{u} \approx \check{\mathbf{u}} = \langle \mathbf{u} \rangle + \sum_{k=1}^{N} x_k \mathbf{v}_k \tag{14}$$

To reconstruct at least all the samples in $\mathbf{D}$, the coefficients $\boldsymbol{\theta}_j$, for $j = 1, \ldots, S$, are evaluated projecting the matrix $\mathbf{P}$ on $\widetilde{\mathbf{Z}}'$, that contains only the first N eigenvectors of $\widetilde{\mathbf{Z}}$, retaining the desired level of variance of the original design space, as follows

$$\boldsymbol{\Theta} = \mathbf{P}^{\mathsf{T}} \widetilde{\mathbf{G}} \widetilde{\mathbf{W}} \widetilde{\mathbf{Z}}' \tag{15}$$

with $\boldsymbol{\Theta} = [\boldsymbol{\theta}_1 \ \ldots \ \boldsymbol{\theta}_S]^{\mathsf{T}}$. Consequently, the reduced design variables $\mathbf{x} = [x_1 \ \ldots \ x_N]^{\mathsf{T}}$ can be bounded such as

$$\min_j \Theta_{jk} \leq x_k \leq \max_j \Theta_{jk} \qquad k = 1, \ \ldots \ N. \tag{16}$$

It may be noted that the overall methodology is independent of the specific shape modification method, which is seen as a black box by PME.

4.2. Supervised Learning via Active Learning-Based Multi-Fidelity Surrogate Modelling

Having an arbitrary number L of fidelity levels and defining their training sets as $\{\mathcal{T}_k\}_{k=1}^{L}$, with each $\mathcal{T}_k = \{(\mathbf{x}'_j, f_k(\mathbf{x}'_j))\}_{j=1}^{\mathcal{J}_k}$, the multi-fidelity approximation $\widehat{f}_k(\mathbf{x})$ of $f(\mathbf{x})$ reads [30]

$$\widehat{f}_k(\mathbf{x}) := \widetilde{f}_L(\mathbf{x}) + \sum_{i=k}^{L-1} \widetilde{\varepsilon}_i(\mathbf{x}), \tag{17}$$

where $\widetilde{f}_L$ is the single-fidelity surrogate model associated to the lowest-fidelity training set, and $\varepsilon_i(\mathbf{x})$ is the inter-level error surrogate with associated training set $\mathcal{E}_i = \{(\mathbf{y}, \phi - \widehat{f}_i(\mathbf{y})) \,|\, (\mathbf{y}, \phi) \in \mathcal{T}_{i-1}\}$ [44].

In this context, the surrogate models are based on stochastic RBFs, whose details can be found in [30]. These provide also the uncertainty associated with the prediction of the lowest-fidelity $U_{\widetilde{f}_L}$ and inter-level errors $U_{\widetilde{\varepsilon}_i}$. Assuming they are uncorrelated, the multi-fidelity approximation $\widehat{f}(\mathbf{x})$ of $f(\mathbf{x})$ and its uncertainty $U_{\widehat{f}}$ read

$$f(\mathbf{x}) \approx \widehat{f}(\mathbf{x}) = \widetilde{f}_L(\mathbf{x}) + \sum_{i=1}^{L-1} \widetilde{\varepsilon}_i(\mathbf{x}) \qquad U_{\widehat{f}}(\mathbf{x}) = \sqrt{U^2_{\widetilde{f}_L}(\mathbf{x}) + \sum_{i=1}^{L-1} U^2_{\widetilde{\varepsilon}_i}(\mathbf{x})}. \tag{18}$$

The multi-fidelity surrogate model is refined by incorporating new training points through an active learning process. These new points, denoted as $\mathbf{x}^\star$, are sequentially identified based on an acquisition function, which in this case is determined using the lower confidence bounding (LCB) criterion [45]. The objective of this criterion is to locate points with high prediction uncertainty and low objective function values. Once the new

point $\mathbf{x}^\star$ is identified, the fidelity level for sampling is automatically selected using a fidelity selection vector, $\boldsymbol{\kappa}$, defined as

$$\boldsymbol{\kappa} \equiv \{U_{\tilde{\varepsilon}_1}/\beta_1, \ldots, U_{\tilde{\varepsilon}_{L-1}}/\beta_{L-1}, U_{\tilde{f}_L}/\beta_L\}, \tag{19}$$

where $\beta_i = c_i/c_1$, $i = 1, \ldots, L$, and c_i represents the computational cost associated with the i-th fidelity level. In the case of a non-nested training set, the fidelity level to sample is determined by finding the maximum value in $\boldsymbol{\kappa}$, as given by

$$k = \text{maxloc}(\boldsymbol{\kappa}) \qquad \text{with} \qquad i = k \tag{20}$$

4.3. Development and Integration Approach

The ML techniques were developed using in-house tools. No external machine learning libraries such as Scikit-learn, TensorFlow, or PyTorch were employed. The algorithms were custom-built to meet the specific needs of the hydrodynamic shape optimization process, allowing for greater flexibility and adaptability in handling the design space and fidelity data. The software environment was designed to integrate seamlessly with the existing optimization workflow, ensuring smooth implementation of the proposed methods. Specifically, the integration between ML tools, optimization algorithms, and numerical solver, is achieved through the exchange of data using ASCII-formatted output files. This modular approach ensures that each component can be connected or disconnected as needed, allowing for flexibility in the design and testing of the optimization framework. This method also facilitates a smooth and straightforward integration between the various solvers and optimization algorithms, ensuring efficient data exchange and communication across the workflow.

Regarding the ML methods setup, it may be noted that the PME and multi-fidelity surrogate model does not rely on traditional hyper-parameters like those found in neural networks or other deep learning models. Instead, the key parameters are associated with the dimensionality reduction process (level of variance to be retained and data set dimension) and the active learning sampling strategy (kind of acquisition function).

5. Results

The multi-fidelity method is trained using CFDShip-Iowa as HF and WARP as LF solvers to optimize resistance for both Problem 1 and Problem 2. For evaluating seakeeping performance in Problem 2, CFDShip-Iowa and SMP are used as HF and LF solvers, respectively. Details of the solver verification and validation can be found in [46]. The computational cost ratio between HF and LF solvers is approximately 0.001, highlighting the potential savings provided by the multi-fidelity approach. The active learning process, using the LCB criterion, and the optimization of Problem 1 are handled by a memetic single-objective deterministic particle swarm optimization (DPSO) algorithm [47,48], while Problem 2 is addressed with a multi-objective DPSO algorithm [49].

Figure 5 provides a comparison of the wave elevation patterns and pressure fields between the high-fidelity (URANS) and low-fidelity (potential flow) solvers for the original hull. While the pressure distributions show reasonable agreement, the wave elevation predicted by the potential flow model tends to under-predict diverging bow waves and over-predict diverging stern waves. Despite this promising overall agreement for multi-fidelity applications, potential flow models have inherent limitations in capturing performance losses due to flow separation, which could occur in specific regions of the design space. This presents a methodological challenge when using potential flow solvers in multi-fidelity supervised learning frameworks, where accurate flow separation modeling is essential.

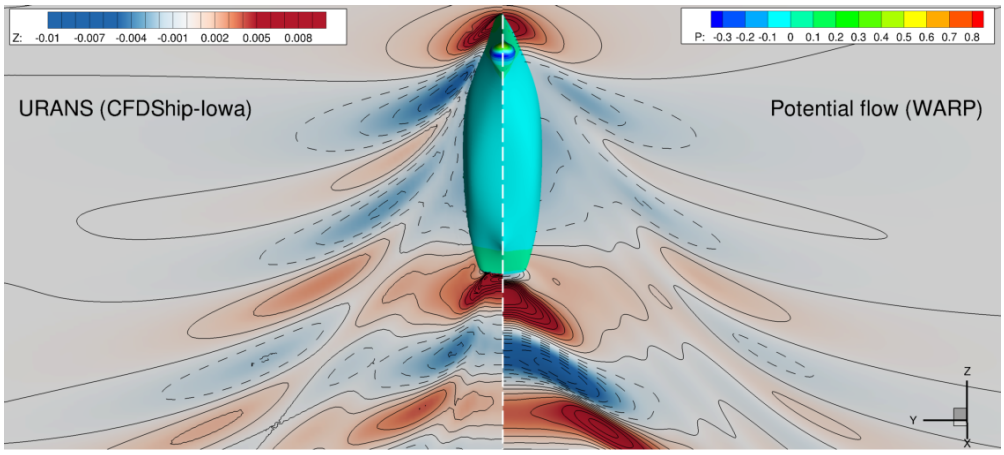

Figure 5. Comparison of URANS (**left**) and PF (**right**) wave elevation pattern and pressure field along the original hull in calm water.

The original FFD design space, consisting of 22 design parameters, undergoes dimensionality reduction via PME. The PME technique is trained using 1000 Monte Carlo realizations, where each realization represents a modified hull configuration along with the corresponding design parameters. The results demonstrate a dimensionality reduction of approximately 70%, reducing the design variables to seven while retaining 95% of the original geometric variance, as shown in Figure 6. This reduction process ensures that the design fidelity is maintained, meaning that the critical geometric features of the original design are retained. Even with fewer design variables, the reduced representation is capable of accurately describing the hull's shape and ensuring its performance remains consistent with the full, high-dimensional design space. This approach not only improves computational efficiency but also allows for effective optimization without compromising the overall quality or accuracy of the design.

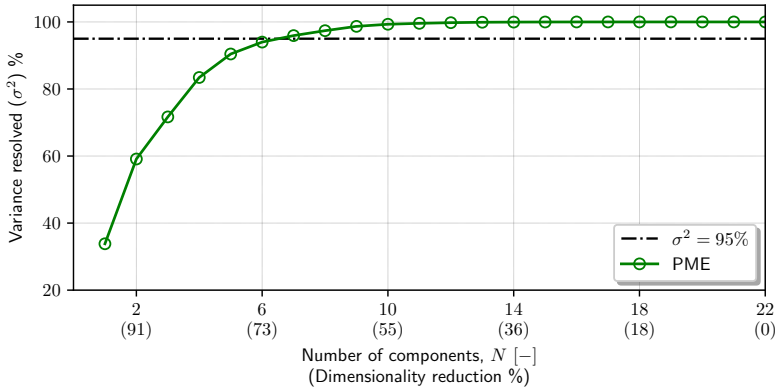

Figure 6. Result of the design-space dimensionality reduction using PME.

The optimization process is initialized with a training set comprising 15 LF and one HF sample at the center of the design domain. Active learning then iteratively refines the surrogate model, stopping once 15 HF samples have been added. Optima for both Problem 1 and Problem 2 are achieved with a total of 15 HF and 647 LF evaluations and validated through a high-fidelity simulation. For Problem 1 (calm water), the optimization leads to a 5.8% reduction in resistance. In Problem 2 (regular waves), the optimization yields a 2.6% reduction in resistance, accompanied by a 6.2% improvement of the SMF. These results are particularly noteworthy, as previous studies [46] have not identified a compromise solution that enhances both resistance and seakeeping performance simultaneously.

Figure 7 shows a comparison of the original hull stations with the optimized designs for both problems. In Problem 1, the optimization primarily affects the stern, with minimal

changes to the forward sections of the hull. The optimized stern geometry results in improved pressure recovery and reduced diverging stern waves, as illustrated in Figure 8. A further investigation of wave patterns is shown in Figure 9, where longitudinal wave cuts at $y = B, 2B, 3B$, and $5B$ are depicted. While the optimized stern geometry has reduced the diverging stern waves, the wave cuts indicate an increase in wave height, suggesting that the optimization, while effective in reducing the total resistance, have shifted the energy distribution in the wave system, leading to higher waves in some regions. On the contrary, for Problem 2, the optimized hull exhibits significant modifications near the forward perpendicular, including an enlarged bow dome, while the aft sections remain relatively unchanged. The optimal hull for Problem 2 is selected as the best trade-off solution from the non-dominated set, balancing the competing objectives of minimizing resistance in waves and enhancing seakeeping performance, as shown in Figure 10 (left). The figure also indicates the HF training points and validates the optimal solution. Figure 10 (center and right) compares the heave and pitch motions between the original and optimized hulls. While the optimization results in a minimal reduction in heave and a good improvement in pitch at the center of gravity, the enlarged bow dome effectively breaks the incoming head waves, leading to the desired reduction in resistance. Further investigation is needed to better understand the impact of these modifications on the overall wave interaction and dynamic stability of the vessel, as well as the complex interaction between the optimized hull shape and resistance components.

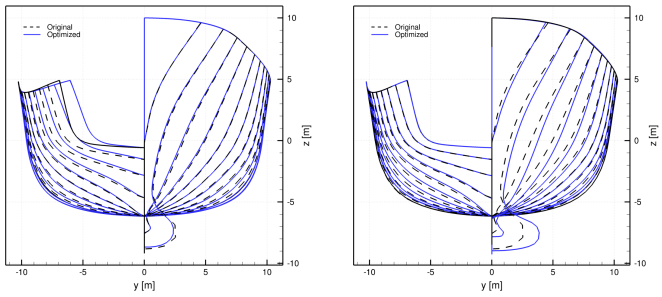

Figure 7. Comparison between the original hull stations and the optimized designs for problem 1 (**left**, single-objective—best resistance in calm water) and problem 2 (**right**, multi-objective—best trade-off between resistance in head waves and seakeeping merit factor).

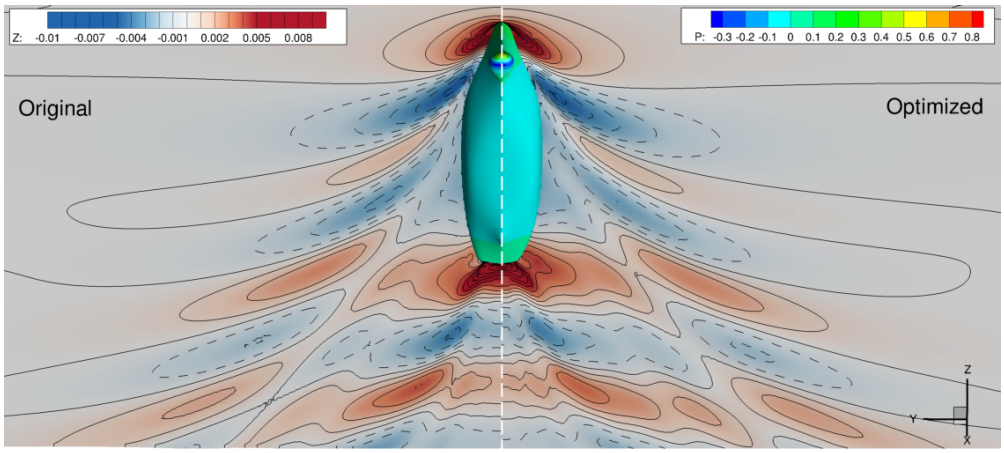

Figure 8. Comparison between the original and optimized wave elevation patterns and pressure fields along the hull for problem 1 obtained with URANS simulations.

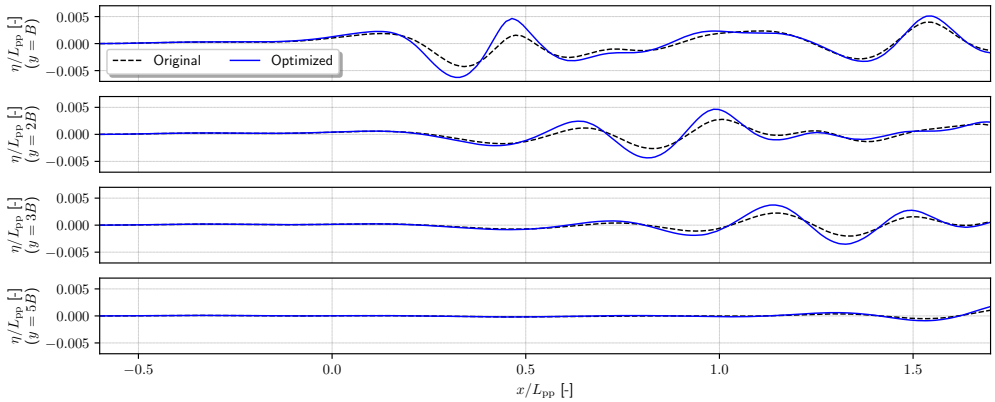

Figure 9. Comparison between the original and optimized longitudinal wave cuts at, from top to bottom, $y = B$, $2B$, $3B$, and $5B$ for problem 1 obtained with URANS simulation.

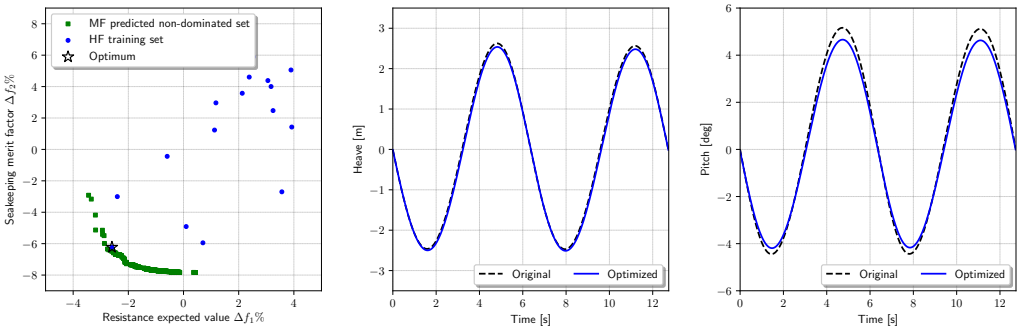

Figure 10. Non-dominated solution set for problem 2 (**left**) and comparison of heave (**center**) and pitch (**right**) motions between the original and optimized hulls.

A final analysis of the active learning-based multi-fidelity optimization results has been carried out to examine the correlation between the different information sources, i.e., the relationship between the predictions provided by high-fidelity and low-fidelity simulations in the multi-fidelity optimization process—each fidelity level represents an information source, and their correlation indicates how well the low-fidelity simulations approximate the results of the high-fidelity ones. Specifically, Figure 11 illustrates the relative variation of the objective functions between the LF and HF training points for both Problem 1 (left) and Problem 2 (right). For Problem 1 (calm water, Figure 11, left), the data show a reasonably good correlation between the two information sources, as indicated by the linear regression line, though not perfect (the black line represents an ideal correlation), achieving a Pearson correlation coefficient $r = 0.803$. This suggests that, for this specific problem, the potential flow model can be quite effective in predicting the objective function when no flow separation occurs. However, large deviations in both under- and overestimation of the objective function may occur, likely due to flow separation phenomena, which the potential flow model cannot accurately capture. In Problem 2 (seakeeping, Figure 11, right), two key observations emerge: (1) the correlation between LF and HF sources is relatively strong for seakeeping performance ($r = 0.854$), indicating that strip theory provides a reasonable approximation when compared to more complex URANS simulations, although there is a slight underestimation of the objective function; (2) unlike Problem 1, the relationship between the potential flow and URANS models tends to be anti-correlated ($r = -0.499$), which suggests a more non-linear interaction between the information sources that is challenging for supervised learning methods to model accurately. This anti-correlation is likely due to the inability of the potential flow model to account for the added resistance component, which plays a crucial role in seakeeping performance.

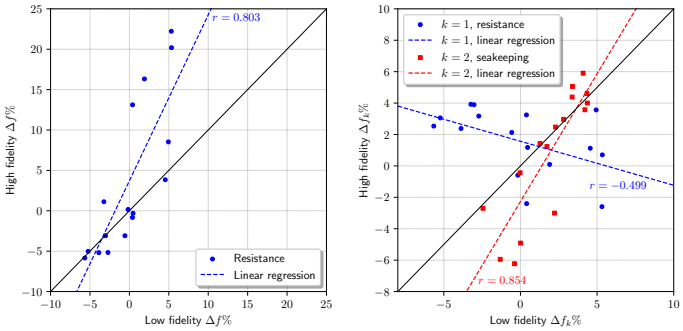

Figure 11. Correlation of objective functions between high-fidelity and low-fidelity numerical solutions (problem 1 on left and problem 2 on right).

6. Conclusions

This paper demonstrates a novel yet practical integration of machine learning techniques into simulation-based design optimization processes for hydrodynamic shape optimization. The key contribution of this work lies in showing that advanced machine learning methods—namely parametric model embedding (PME) for dimensionality reduction and active learning-based multi-fidelity surrogate modeling—can be seamlessly incorporated into existing optimization workflows without the need for significant modifications to the toolchain. This ensures that these innovations can be adopted without disrupting current design processes, providing an accessible path to significant improvements in efficiency and performance.

Through the application of single- and multi-objective optimization techniques on the DTMB 5415 model, it was shown that machine learning methods offer promising solutions to the challenges associated with high-dimensional design spaces and the computational costs of high-fidelity simulations. The use of PME, which extends the standard PCA approach, enabled significant dimensionality reduction, addressing the curse of dimensionality while preserving the most relevant design characteristics. This is particularly valuable as it facilitates optimization in reduced spaces without the need for complex reparameterizations. The active learning-based multi-fidelity surrogate modeling, on the other hand, enhances the optimization process by dynamically guiding both the sampling locations and the fidelity level, balancing computational cost with prediction uncertainty. This approach significantly reduces the reliance on high-fidelity simulations, providing an innovative yet practical solution to the challenges posed by high-dimensional design spaces.

An estimated cost reduction between 65% and 98% was achieved by reducing the design space from 22 to 7 dimensions using PME and constructing a multi-fidelity surrogate model with 15 high-fidelity and 647 low-fidelity simulations, where the latter come at 0.1% of the cost of a high-fidelity simulation. The 65% cost reduction was calculated by comparing the multi-fidelity approach, which used 15 high-fidelity points following a $2N + 1$ rule (with $N = 7$ in the reduced space), to a scenario in the original design space that would have required 45 high-fidelity points to achieve a similar sampling density. The upper bound of 98% reflects the cost savings compared to a scenario using only 647 high-fidelity simulations. Without these techniques, significantly more high-fidelity simulations would have been required to adequately explore the original high-dimensional space, demonstrating the computational efficiency provided by this approach.

The results presented in this paper demonstrate the practical benefits of integrating machine learning into hydrodynamic shape optimization, offering a path toward more efficient and streamlined optimization processes. Beyond the computational savings, this approach introduces a new methodology for tackling high-dimensional optimization problems, which are common in engineering design. By reducing the reliance on high-fidelity simulations and accelerating the design process, the proposed framework offers a practical and scalable solution for optimizing ship hydrodynamics. These advances are not only relevant to naval applications but could also be extended to other fields such as aerospace

and automotive engineering, where the optimization of complex geometries plays a central role. Moreover, the framework aligns with the growing need for sustainable engineering solutions by reducing computational resources and enabling faster design iterations, which are critical for minimizing time-to-market and improving overall performance.

Future work should explore the extension of these techniques to more complex design scenarios and further investigate the application of machine learning for uncertainty quantification in naval design.

Author Contributions: Conceptualization, A.S. and M.D.; methodology, A.S. and M.D.; software, A.S.; formal analysis, A.S.; investigation, A.S.; writing—original draft preparation, A.S.; writing—review and editing, A.S. and M.D.; visualization, A.S.; supervision, M.D.; funding acquisition, M.D. All authors have read and agreed to the published version of the manuscript.

Data Availability Statement: Data are contained within the article.

Acknowledgments: The work is conducted in collaboration with the NATO task group AVT-331 on "Goal-driven, multi-fidelity approaches for military vehicle system-level design". Authors are supported by the Office of Naval Research (ONR) and ONR Global, Program Officers Woei-Min Lin and Elena McCarthy, through grants N62909-18-1-2033 and N62909-21-1-2042 and acknowledge the support of the Italian Ministry of University and Research (MUR) through the National Recovery and Resilience Plan (PNRR), Sustainable Mobility Center (CNMS), Spoke 3 Waterways, CN00000023-CUP B43C22000440001.

Conflicts of Interest: The authors declare no conflict of interest. The funders had no role in the design of the study; in the collection, analyses, or interpretation of data; in the writing of the manuscript, or in the decision to publish the results.

Nomenclature

f	Objective function
$\hat{f}$	Multi-fidelity surrogate model approximation
$\tilde{\varepsilon}$	Inter-level error surrogate
$\mathbf{d}$	Discretized shape modification vector
$\mathbf{g}, \mathbf{g}'$	Original and deformed geometry
$\mathbf{u}$	Vector of original design variables
$\mathbf{x}$	Vector of reduced design variables
$\mathbf{v}_k$	PME eigenvectors associated to $\mathbf{u}$
$\mathbf{z}_k$	PME eigenvectors associated to $\mathbf{d}$
$\mathbf{P}$	PME data matrix
$\widetilde{\mathbf{W}}$	PME weights matrix
$\widetilde{\mathbf{Z}}$	PME eigenvectors matrix
M	Number of original design variables
N	Number of reduced design variables

References

1. Joung, T.H.; Kang, S.G.; Lee, J.K.; Ahn, J. The IMO initial strategy for reducing Greenhouse Gas (GHG) emissions, and its follow-up actions towards 2050. *J. Int. Marit. Saf. Environ. Aff. Shipp.* **2020**, *4*, 1–7.
2. Serani, A.; Scholcz, T.P.; Vanzi, V. A scoping review on simulation-based design optimization in marine engineering: Trends, best practices, and gaps. *Arch. Comput. Methods Eng.* **2024**, https://doi.org/10.1007/s11831-024-10127-1.
3. Li, J.; Du, X.; Martins, J.R. Machine learning in aerodynamic shape optimization. *Prog. Aerosp. Sci.* **2022**, *134*, 100849.
4. Martić, I.; Degiuli, N.; Grlj, C.G. Prediction of added resistance of container ships in regular head waves using an artificial neural network. *J. Mar. Sci. Eng.* **2023**, *11*, 1293.
5. Yildiz, B. Prediction of residual resistance of a trimaran vessel by using an artificial neural network. *Brodogr. Int. J. Nav. Archit. Ocean Eng. Res. Dev.* **2022**, *73*, 127–140.
6. Diez, M.; Gaggero, M.; Serani, A. Data-driven forecasting of ship motions in waves using machine learning and dynamic mode decomposition. *Int. J. Adapt. Control Signal Process.* **2024**, https://doi.org/10.1002/acs.3835.
7. Ozsari, I. Predicting main engine power and emissions for container, cargo, and tanker ships with artificial neural network analysis. *Brodogr. Int. J. Nav. Archit. Ocean Eng. Res. Dev.* **2023**, *74*, 77–94.
8. Mentes, A.; Yetkin, M. An application of soft computing techniques to predict dynamic behaviour of mooring systems. *Brodogr. Int. J. Nav. Archit. Ocean Eng. Res. Dev.* **2022**, *73*, 121–137.

9. Serani, A.; Diez, M. Parametric model embedding. *Comput. Methods Appl. Mech. Eng.* **2023**, *404*, 115776.
10. Bellman, R. *Dynamic Programming*; Princeton University Press: Princeton, NJ, USA, 1957; pp. 4–9.
11. Spinosa, E.; Pellegrini, R.; Posa, A.; Broglia, R.; De Biase, M.; Serani, A. Simulation-Driven design optimization of a destroyer-type vessel via multi-fidelity supervised active learning. *J. Mar. Sci. Eng.* **2023**, *11*, 2232.
12. Di Fiore, F.; Nardelli, M.; Mainini, L. Active learning and bayesian optimization: A unified perspective to learn with a goal. *Arch. Comput. Methods Eng.* **2024**, https://doi.org/10.1007/s11831-024-10064-z.
13. Volpi, S.; Diez, M.; Gaul, N.J.; Song, H.; Iemma, U.; Choi, K.; Campana, E.F.; Stern, F. Development and validation of a dynamic metamodel based on stochastic radial basis functions and uncertainty quantification. *Struct. Multidiscip. Optim.* **2015**, *51*, 347–368.
14. Begovic, E.; Mortola, G.; Incecik, A.; Day, A. Experimental assessment of intact and damaged ship motions in head, beam and quartering seas. *Ocean Eng.* **2013**, *72*, 209–226.
15. Ahmed, Y.M. Numerical simulation for the free surface flow around a complex ship hull form at different Froude numbers. *Alex. Eng. J.* **2011**, *50*, 229–235.
16. Peri, D.; Campana, E.F. Multidisciplinary design optimization of a naval surface combatant. *J. Ship Res.* **2003**, *47*, 1–12.
17. Serani, A.; Fasano, G.; Liuzzi, G.; Lucidi, S.; Iemma, U.; Campana, E.F.; Stern, F.; Diez, M. Ship hydrodynamic optimization by local hybridization of deterministic derivative-free global algorithms. *Appl. Ocean Res.* **2016**, *59*, 115–128.
18. Sun, Z.; Sun, L.y.; Xu, L.x.; Hu, Y.l.; Zhang, G.y.; Zong, Z. A CFD-Based Data-Driven Reduced Order Modeling Method for Damaged Ship Motion in Waves. *J. Mar. Sci. Eng.* **2023**, *11*, 686.
19. Irvine, M. Pitch and heave tests and uncertainty assessment for a surface combatant in regular head waves. *J. Ship Res.* **2008**, *52*, 146–163.
20. Bhushan, S.; Xing, T.; Carrica, P.; Stern, F. Model-and full-scale URANS simulations of Athena resistance, powering, seakeeping, and 5415 maneuvering. *J. Ship Res.* **2009**, *53*, 179–198.
21. Tahara, Y.; Peri, D.; Campana, E.F.; Stern, F. Computational fluid dynamics-based multiobjective optimization of a surface combatant using a global optimization method. *J. Mar. Sci. Technol.* **2008**, *13*, 95–116.
22. Gokce, M.K.; Kinaci, O.K. Numerical simulations of free roll decay of DTMB 5415. *Ocean Eng.* **2018**, *159*, 539–551.
23. Bhushan, S.; Yoon, H.; Stern, F.; Guilmineau, E.; Visonneau, M.; Toxopeus, S.; Simonsen, C.; Aram, S.; Kim, S.; Grigoropoulos, G. Assessment of computational fluid dynamic for surface combatant 5415 at straight ahead and static drift β = 20 deg. *J. Fluids Eng.* **2019**, *141*, 051101.
24. D'Agostino, D.; Serani, A.; Diez, M. Design-space assessment and dimensionality reduction: An off-line method for shape reparameterization in simulation-based optimization. *Ocean Eng.* **2020**, *197*, 106852.
25. Silva, K.M.; Maki, K.J. Data-Driven system identification of 6-DoF ship motion in waves with neural networks. *Appl. Ocean Res.* **2022**, *125*, 103222.
26. Mancini, S.; Begovic, E.; Day, A.H.; Incecik, A. Verification and validation of numerical modelling of DTMB 5415 roll decay. *Ocean Eng.* **2018**, *162*, 209–223.
27. Longo, J.; Stern, F. Uncertainty assessment for towing tank tests with example for surface combatant DTMB model 5415. *J. Ship Res.* **2005**, *49*, 55–68.
28. Yoon, H.; Simonsen, C.D.; Benedetti, L.; Longo, J.; Toda, Y.; Stern, F. Benchmark CFD validation data for surface combatant 5415 in PMM maneuvers–Part I: Force/moment/motion measurements. *Ocean Eng.* **2015**, *109*, 705–734.
29. Liu, X.; Zhao, W.; Wan, D. Multi-fidelity Co-Kriging surrogate model for ship hull form optimization. *Ocean Eng.* **2022**, *243*, 110239.
30. Pellegrini, R.; Wackers, J.; Broglia, R.; Serani, A.; Visonneau, M.; Diez, M. A multi-fidelity active learning method for global design optimization problems with noisy evaluations. *Eng. Comput.* **2023**, *39*, 3183–3206.
31. Beran, P.S.; Bryson, D.; Thelen, A.S.; Diez, M.; Serani, A. Comparison of multi-fidelity approaches for military vehicle design. In Proceedings of the AIAA AVIATION 2020 FORUM, virtual, 15–19 June 2020; p. 3158.
32. Sederberg, T.W.; Parry, S.R. Free-form deformation of solid geometric models. In Proceedings of the 13th Annual Conference on Computer Graphics and Interactive Techniques, Dallas, TX, USA, 18–22 August 1986; pp. 151–160.
33. Grigoropoulos, G.; Campana, E.F.; Diez, M.; Serani, A.; Goren, O.; Sarioz, K.; Danisman, D.; Visonneau, M.; Queutey, P.; Abdel-Maksoud, M.; et al. Mission-based hull-form and propeller optimization of a transom stern destroyer for best performance in the sea environment. In Proceedings of the VII International Congress on Computational Methods in Marine Engineering-MARINE, Nantes, France, 15–17 May 2017.
34. Huang, J.; Carrica, P.M.; Stern, F. Semi-coupled air/water immersed boundary approach for curvilinear dynamic overset grids with application to ship hydrodynamics. *Int. J. Numer. Methods Fluids* **2008**, *58*, 591–624.
35. Bell, J.; Howell, L.; Colella, P. An efficient second-order projection method for viscous incompressible flow. In Proceedings of the 10th Computational Fluid Dynamics Conference, Honolulu, HI, USA, 24–26 June 1991; p. 1560.
36. Noack, R. SUGGAR: A general capability for moving body overset grid assembly. In Proceedings of the 17th AIAA Computational Fluid Dynamics Conference, Toronto, ONT, Canada, 6–9 June 2005; p. 5117.
37. Dawson, C.W. A practical computer method for solving ship-wave problems. In Proceedings of the 2nd International Conference on Numerical Ship Hydrodynamics, Berkeley, CA, USA, 19–21 September 1977; pp. 30–38.
38. Schlichting, H.; Gersten, K. *Boundary-Layer Theory*; Springer: Berlin/Heidelberg, Germany, 2000.

39. Bassanini, P.; Bulgarelli, U.; Campana, E.F.; Lalli, F. The wave resistance problem in a boundary integral formulation. *Surv. Math. Ind.* **1994**, *4*, 151–194.
40. Meyers, W.G.; Baitis, A.E. *SMP84: Improvements to Capability and Prediction Accuracy of the Standard Ship Motion Program SMP81*; Technical Report SPD-0936-04; David Taylor Naval Ship Research and Development Center: Bethesda, MD, USA, 1985.
41. Wackers, J.; Pellegrini, R.; Serani, A.; Visonneau, M.; Diez, M. Efficient initialization for multi-fidelity surrogate-based optimization. *J. Ocean Eng. Mar. Energy* **2023**, *9*, 291–307.
42. Diez, M.; Campana, E.F.; Stern, F. Design-space dimensionality reduction in shape optimization by Karhunen–Loève expansion. *Comput. Methods Appl. Mech. Eng.* **2015**, *283*, 1525–1544.
43. Serani, A.; Diez, M. A Survey on Design-space Dimensionality Reduction Methods for Shape Optimization. *arXiv* **2024**, arXiv:2405.13944.
44. Piazzola, C.; Tamellini, L.; Pellegrini, R.; Broglia, R.; Serani, A.; Diez, M. Comparing multi-index stochastic collocation and multi-fidelity stochastic radial basis functions for forward uncertainty quantification of ship resistance. *Eng. Comput.* **2023**, *39*, 2209–2237.
45. Serani, A.; Pellegrini, R.; Wackers, J.; Jeanson, C.E.; Queutey, P.; Visonneau, M.; Diez, M. Adaptive multi-fidelity sampling for CFD-based optimisation via radial basis function metamodels. *Int. J. Comput. Fluid Dyn.* **2019**, *33*, 237–255.
46. Serani, A.; Stern, F.; Campana, E.F.; Diez, M. Hull-form stochastic optimization via computational-cost reduction methods. *Eng. Comput.* **2022**, *38*, 2245–2269.
47. Serani, A.; Diez, M.; Campana, E.F.; Fasano, G.; Peri, D.; Iemma, U. Globally Convergent Hybridization of Particle Swarm Optimization Using Line Search-Based Derivative-Free Techniques. In *Recent Advances in Swarm Intelligence and Evolutionary Computation*; Yang, X.S., Ed.; Studies in Computational Intelligence; Springer: Berlin/Heidelberg, Germany, 2015; Volume 585, pp. 25–47.
48. Serani, A.; Leotardi, C.; Iemma, U.; Campana, E.F.; Fasano, G.; Diez, M. Parameter selection in synchronous and asynchronous deterministic particle swarm optimization for ship hydrodynamics problems. *Appl. Soft Comput.* **2016**, *49*, 313–334.
49. Pellegrini, R.; Serani, A.; Leotardi, C.; Iemma, U.; Campana, E.F.; Diez, M. Formulation and parameter selection of multi-objective deterministic particle swarm for simulation-based optimization. *Appl. Soft Comput.* **2017**, *58*, 714–731.